PHOTONICS Research

Solution-processed halide perovskite microcavity exciton-polariton light-emitting diodes working at room temperature

Tianyu Liu,[1] Peng Ran,[1] Yirong Su,[1] Zeng Chen,[2] Renchen Lai,[3] Weidong Shen,[1] Yaoguang Ma,[1] Haiming Zhu,[2] and Yang (Michael) Yang[1,*]

[1]State Key Laboratory of Modern Optical Instrumentation, Institute for Advanced Photonics, College of Optical Science and Engineering, Zhejiang University, Hangzhou 310027, China
[2]State Key Laboratory of Modern Optical Instrumentation, Key Laboratory of Excited State Materials of Zhejiang Province, Department of Chemistry, Zhejiang University, Hangzhou 310027, China
[3]Instrumentation and Service Center for Molecular Sciences, Westlake University, Hangzhou 310024, China
*Corresponding author: yangyang15@zju.edu.cn

Received 22 June 2023; revised 1 August 2023; accepted 7 August 2023; posted 8 August 2023 (Doc. ID 498412); published 1 October 2023

Exciton-polaritons offer the potential to achieve electrically pumped perovskite polariton lasers with much lower current thresholds than conventional photonic lasers. While optically pumped exciton-polaritons have been widely studied in halide perovskites, electrically-pumped polaritons remain limited. In this study, we demonstrate the use of a solution-processing strategy to develop halide perovskite polariton light-emitting diodes (LEDs) that operate at room temperature. The strong coupling of excitons and cavity photons is confirmed through the dispersion relation from angle-resolved reflectivity, with a Rabi splitting energy of 64 meV. Our devices exhibit angle-resolved electroluminescence following the low polariton branch and achieve external quantum efficiencies of 1.7%, 3.85%, and 3.7% for detunings of 1.1, −77, and −128 meV, respectively. We also explore devices with higher efficiency of 5.37% and a narrower spectral bandwidth of 6.5 nm through the optimization of a top emitting electrode. Our work demonstrates, to our knowledge, the first room-temperature perovskite polariton LED with a typical vertical geometry and represents a significant step towards realizing electrically pumped perovskite polariton lasers.

https://doi.org/10.1364/PRJ.498412

1. INTRODUCTION

The exciton–polariton is a hybrid quasiparticle that emerges from the strong coupling between excitons and cavity photons, exhibiting unique properties such as low effective mass, strong nonlinearity, and macroscopic propagation [1–3]. A wide range of exciton-polariton devices have been developed, including polariton transistors and gates [4,5], polariton lasers [6], optically controlled interferometers [7], and polariton current qubits [8]. Particularly, polaritons can condense to a single quantum state, forming Bose–Einstein condensates and emitting coherent light with a much lower threshold than traditional photonic lasing. This characteristic enables new opportunities for realizing electrically pumped polariton lasers, which may be suitable for emerging excitonic emitters that often exhibit tremendous optoelectronic properties but are relatively fragile. Among these, halide perovskite semiconductors are very attractive due to their high luminescence efficiency, tunable spectrum, high optical gain, high carrier mobility, and scalable solution processability. However, perovskite semiconductors face challenges in reaching the current threshold for photonic lasers, which is typically between 10^4 and 10^5 A/cm^2 [9–11], due to ion migration or stability issues. Polariton lasing offers a promising alternative solution, with a current threshold of about two to three orders of magnitudes lower than that of photonic lasing [12,13] and therefore within the attainable range of perovskite electroluminescence (EL) devices [14,15].

In fact, halide perovskite has already proven to be a promising material for polariton devices at room temperature (RT), owing to its unique features such as stable excitons at RT, large oscillator strength, narrow exciton linewidth, and outstanding optical properties [1,3]. A plethora of achievements have already been made in halide perovskite polariton photonics under optical pumping, including polariton lasing [16–18], RT condensate flow [19,20], spin–orbit coupling [21–23], one-dimensional polariton lattices [24], polaritonic vortices [25], and polariton parametric oscillators [26]. Based on the development history of other material systems such as GaAs [27–30], GaN [31], ZnO [32–36], and organic [37–41] and transition metal dichalcogenides (TMDs) [42], the next step towards electrically

pumped exciton-polariton lasing is generally believed to be the realization of a polariton light-emitting diode (LED) operating in the strong-coupling regime. However, electrically pumped perovskite polariton devices are still much less explored. Currently, only one small-scale perovskite polariton EL device has been demonstrated under 7 K by using chemical vapor deposited single crystalline perovskite [43]. Therefore, there is a critical need to develop RT perovskite polariton LED devices with a typical vertical emitting diode structure. Given that the exciton–polariton can be optically pumped in solution-processed polycrystalline $MAPbBr_3$ [44], polariton LEDs should be achievable. However, several issues still need to be addressed, including (i) the selection of an appropriate perovskite component to spontaneously obtain strong optical coupling and sufficient EL performance, (ii) collaborative optimization of electrical functional layers and multilayer optical microcavities, and (iii) accurate control of the thickness and morphology of the solution-processed perovskite.

In this work, we combined solution-processed $CsPbBr_3$ LED devices with metal–dielectric planar mirrors to demonstrate top-emitting microcavity polariton LEDs. Strong coupling has been confirmed through the anticrossing behavior in a dispersion relation resulting in a Rabi splitting of 64 meV. Additionally, angle-resolved EL (AREL) has been observed following the low polariton (LP) branch dispersion, complemented by photoluminescence (PL) at different detunings.

2. EXPERIMENT

A. Materials

Cesium bromide (CsBr, 99.999%), lead (II) bromide ($PbBr_2$, 99.999%), lithium bromide (LiBr, 99.999%), and poly-(N-vinylcarbazole) (PVK, average Mn 25,000–50,000) were purchased from Sigma Aldrich. 1,4,7,10,13,16-hexaoxacyclooctadecane (18-crown-6, 98%) was purchased from Acros. Poly[(9,9-dioctylfluorenyl-2,7-diyl)-co-(4,4'-(N-(4-sec-butylphenyl) diphenyl-amine)] (TFB, Mw > 30,000) was purchased from Luminescence Technology Corp. Nickel(II) acetate tetrahydrate (99%) and ethyl alcohol (99.5%) were purchased from Aladdin. Dimethyl sulfoxide (DMSO, 99.7%) and chlorobenzene (99.8%, extra dry) were purchased from J&K Scientific. Toluene (HPLC) was purchased from TEDIA. 2,2',2''-(1,3,5-Benzinetriyl)-tris(1-phenyl-1-H-benzimidazole) (TPBi, 99.5%, sublimed) was purchased from Jilin OLED Material Tech Co., Ltd. Lithium fluoride (LiF, 99%) was purchased from Xi'an Polymer Light Technology Corp. Mg and Ag (evaporation slug) were purchased from Fuzhou Invention photoelectrical Technology. All the chemical materials were directly used without any further purifications.

B. Device Fabrication

Preparations of the dielectric mirrors and substrates: TiO_2/SiO_2 stack films were deposited on a glass substrate by electron beam evaporation, including the multi-layer distributed Bragg reflector (DBR) and a 120 nm SiO_2 spacer. The central wavelength of DBR was set to 520 nm. Indium tin oxide (ITO) film was sputtered on a TiO_2/SiO_2 substrate at a temperature of 300°C with a shadow mask of 0.1 mm thickness. The TiO_2/SiO_2/ITO substrates were washed in ultrasonic cleaner and treated by UV ozone for 30 min to make the surface more hydrophilic.

NiO_x precursor solution: We dissolved 124.4 mg of $Ni(CH_3COO)_2 \cdot 4H_2O$ in 5 mL of ethanol, and added a drop of hydrochloric acid (about 50 μL) into the solution. We stirred the solution at RT overnight, and then filtered it three times using 0.22 μm hydrophobic polytetrafluoroethylene (PTFE) syringe filters.

Perovskite precursor solution: We dissolved CsBr, PbBr, and LiBr in DMSO with a molar ratio of 1.1:1:0.2 to obtain a $CsPbBr_3$ solution containing 0.45 mol/L Pb^{2+}. We added 27 mg/mL crown to the perovskite precursor solution and stirred it at RT overnight. Prior to use, we filtered the precursor solution using 0.22 μm PTFE syringe filters.

LED devices preparation: To prepare the LED devices, we first spin-coated NiO_x solution onto an ITO substrate at 4000 r/min for 30 s, and baked it at 300°C for 30 min in ambient air. The substrate was then transferred to a N_2-filled glovebox. Next, we deposited the TFB layers by spinning the solution (8 mg/mL in chlorobenzene) at 2000 r/min for 30 s and annealing at 150°C for 30 min. The PVK layers (4 mg/mL in toluene) were then spin-coated at 4000 r/min on the TFB films, followed by annealing at 150°C for 30 min. For the perovskite films, we used a two-step solution spin-coating process at 1000 r/min for 5 s and 3000 r/min for 85 s. The resulting $CsPbBr_3$ film was then annealed at 100°C for 10 min. Subsequently, we evaporated TPBi (1 Å/s) and LiF (0.3 Å/s) sequentially on the as-prepared perovskite films in a thermal evaporator under 3.0×10^{-6} Torr. Finally, we prepared the Mg:Ag (1 nm) and Ag (MAA) cathode using a co-evaporation method with evaporating rates of 1:0.1 Å/s and 0.8 Å/s, respectively. The device area was defined as the overlapping area of the ITO and MAA electrode, with dimensions of 1.5 mm × 2 mm.

C. Characterizations

Several characterization techniques were employed to measure various properties of the films. The thickness was measured using a surface profiler (DEKTAK-XT, Bruker). A cross-sectional image was obtained from a field emission scanning electron microscope (Ultra 55, Zeiss) operated at 5 kV. Surface roughness was determined by atomic force microscopy (AFM) (Oxford Cypher S, Asylum Research) inside a nitrogen-filled glove box. Temperature-dependent PL measurements were conducted by FLS 1000 (Edinburgh Instruments) with a temperature controller MercuryiTC (Oxford Instruments). PL mapping was performed by confocal microscopy (Nikon C2 + Confocal System, Nikon Instruments Inc.), where the sample was excited by a 405 nm laser diode, and the scan intensity was recorded by an avalanche photodiode (SPCM-AQR-16-FC from PerkinElmer). Micro-area PL spectra were recorded by a spectrometer (QEPro, Ocean Optics). Angular reflectivity and absorption spectra were measured using a UV-VIS spectrophotometer (Cary 7000, Agilent). Normal reflectivity was measured using a homemade system consisting of a Y-type fiber, reflection probe, halogen lamp, and spectrometer, as shown in Appendix A Fig. 6. Reflectivity spectra were obtained by comparing the sample with a reference silver mirror. Angle-dependent steady-state PL/EL spectra were obtained by using a spectrometer (QEPro, Ocean Optics) and a fiber probe at a

fixed distance of 15 cm from the sample. For PL measurement, a 405 nm 20 mW laser diode, attenuated by a neutral density filter, was used as the excitation source. For EL measurement, a 0.26 mA current output from a Keithley 2400 source meter was supplied to the devices during the measurement process. The schematic diagram of angle-dependent steady-state PL/EL setups is shown in Ref. [45]. *J-V-L*-external quantum efficiency (EQE) curves were characterized using a large diameter Si detector (10 mm) operated at 0 V to measure the output power of devices. The detector was placed in contact with the active pixel as much as possible and underfilled the detector area, while scanning voltage and monitoring the current by the Keithley 2400 source meter simultaneously in a nitrogen-filled glove box. Luminance was calculated using the spectrum and photocurrent of the Si detector. The EQE was calculated by converting the detector current signal to emitted photons and the device current to electrons. All the devices tested in ambient air were encapsulated by glass with UV-cured resin (TB3031B, Threebond).

D. Simulations and Data Fitting

To simulate the optical field distribution of the device, a MATLAB program developed by McGehee Group [46] was used to perform transfer matrix optical modeling. The dispersion curves and photonic/excitonic weights of the exciton–polariton were then calculated and fitted using Eqs. (1) and (2) in MATLAB.

3. RESULTS AND DISCUSSION

A. Structure of the Perovskite Exciton–Polariton LED

The structure of our perovskite exciton–polariton LED is illustrated in Fig. 1(a). Our device is a perovskite LED structure embedded in a Fabry–Perot optical microcavity, where the excitons in the $CsPbBr_3$ film strongly couple with cavity photons, enabling the device to operate in electroluminescent mode with continuous exciton injection from electrical functional layers. The sequential fabrication process is presented in Appendix A Fig. 5. The devices adopt a top-emitting structure. DBR consists of 5.5 pairs of TiO_2/SiO_2 alternate films that act as a total reflection cavity mirror, followed by a 120 nm thick SiO_2 film spacer to compensate for cavity length. The reflectivity of the TiO_2/SiO_2 substrate is measured at 6° as shown in Appendix B Fig. 7(a), with a reflective stopband from 460 nm (2.69 eV) to 600 nm (2.07 eV) covering the whole emission band of $CsPbBr_3$ and centered at 520 nm (2.38 eV) with a value of 98.6%. The transparent ITO anode is patterned by sputtering with an ultrathin mask, whose edge slope zone is 1/20 of the device area, as shown in Appendix B Fig. 7(b), to minimize the edge effect. Detuning values (Δ) from the difference between normal cavity mode photon energy [$E_{ph}(0°)$] and exciton energy (E_x) are adjusted by changing the thickness of ITO. For hole injection, we used three stacked films of NiO_x/TFB/PVK. Spin-coated $CsPbBr_3$ film serves as the emission layer, which interacts with the microcavity. TPBi and LiF films are used as the electron transport layer and electron injection layer, respectively. A semitransparent thin Ag film serves as a cathode, as well as another microcavity mirror for light extraction. Compared to commonly used Al electrodes, Ag films have lower absorption coefficients. To match the electron injection level, a 1 nm Mg:Ag co-evaporation film is inserted between LiF and Ag film to modify the cathode's work function [49,50], forming an MAA alloy cathode. A well-defined layer-by-layer structure of our device is verified by the cross-sectional SEM in Fig. 1(b), where the thicknesses of TiO_2, SiO_2, SiO_2 spacer, ITO, NiO_x, TFB/PVK, $CsPbBr_3$, TPBi, LiF, and MAA

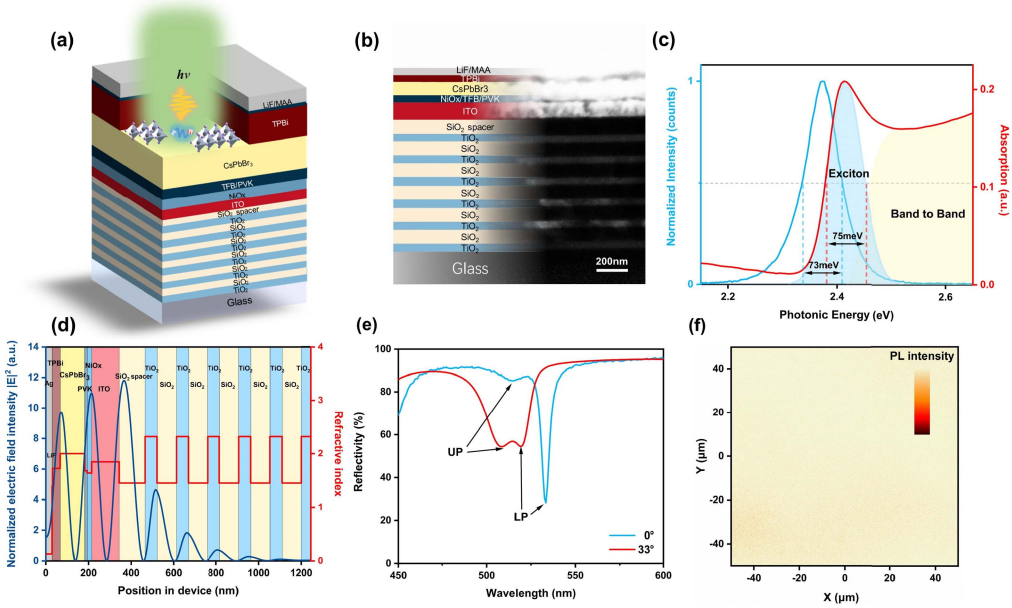

Fig. 1. Structure of the device and basic properties. (a) Schematic structure architecture; (b) cross section scanning electron microscope (SEM) image of the device; (c) normalized emission (blue) and absorption (red) of prepared $CsPbBr_3$ film; (d) refractive index of each layer and electric field distribution of the 530 nm optical standing wave inside device; (e) reflectivity of strongly coupled microcavity device at 0° and 33° relative to the normal direction; (f) PL intensity map of the cavity device with the area of 100 μm × 100 μm.

films are 56, 90, 120, 120, 20, 10, 110, 40, 1, and 30 nm, respectively.

The $CsPbBr_3$ films were characterized by various analyses. X-ray diffraction (XRD) patterns in Appendix B Fig. 7(c) show stronger diffraction peaks for (100), (110), and (200) crystal planes of $CsPbBr_3$, indicating the high crystallinity of the films. The AFM image in Appendix B Fig. 7(d) reveals that the spin-coated $CsPbBr_3$ film has a relatively smooth surface with root mean square (RMS) roughness of 1.737 nm, which can help reduce scattering loss in the cavity. Moreover, with the passivation of LiBr [47], the film samples exhibit bright fluorescence under UV light illumination, as shown in the inset photo of Appendix B Fig. 7(e). From the emission and absorption spectra as shown Fig. 1(c), we can find that an obvious excitonic absorption peak E_x is located at 2.412 eV, and the emission peak is at 2.374 eV, resulting in a Stokes shift of 38 meV. The full-width at half-maximum (FWHM) of the emission and excitonic absorption spectra is 73 and 75 meV, respectively. The exciton absorption can dominate the cavity loss when the $CsPbBr_3$ film is sufficiently thick. Furthermore, we derived the exciton binding energy (E_b) of 47.6 meV by fitting the temperature-dependent PL as shown in Appendix B Figs. 7(e) and 7(f), which is larger than the RT thermal fluctuation energy (≈26 meV), proving the steady existing excitons in $CsPbBr_3$ at RT. These values are consistent with those reported in other studies [47,48].

Taking the −77 meV detuning ($\Delta = -77$ meV) device as an example, we simulated the internal light field distribution at a reference wavelength (λ) of 530 nm, which is presented in Fig. 1(d). The standing wave field between the DBR and Ag indicates a $3\lambda/2$ microcavity, wherein $CsPbBr_3$ film occupies almost $3\lambda/8$ of the optical path, including an antinode and a node. The reflectivity spectrum was initially measured at the normal direction (0°) shown in Fig. 1(e). Two distinct dips were observed at 514.5 nm (2.41 eV) and 533.4 nm (2.32 eV), which correspond to the up polariton (UP) and LP branches, respectively. The coupling of $CsPbBr_3$ excitons to the cavity mode is responsible for these polariton branches. As the angle increased to 33°, the dips shifted to 508 nm (2.44 eV) and 519 nm (2.39 eV), respectively. Additionally, the 100 μm × 100 μm scale PL intensity map presented in Fig. 1(f) demonstrates the uniform spatial distribution of microcavity emission. The PL spectra of the subregions show negligible spectral differences [see Appendix B Figs. 7(g)–7(i)]. These results indicate that our fabrication process ensures the spatial consistency of the resonant mode, which is technically one of the key factors to realize exciton–polariton LEDs.

B. Angular Dispersion from Reflectivity Measurement

To confirm that the device is working in the strong-coupling regime, we measured the angle-resolved reflectivity (ARR) for three different detunings of the microcavity ($\Delta = 1.1$, −77, −128 meV). In each image shown in Fig. 2(a), two dispersion branches can be observed. The energy positions, dips reflectivities, and mode widths of these two branches are related to the detuning values and angle dependent shifts of reflection dips. Most importantly, a characteristic anticrossing between these two branches is revealed, which is a fundamental signature of the strong-coupling regime. All the reflection dips are derived to fit by eigenvalues [Eq. (1)] of a coupled oscillator model for exciton and photon coupling [51,52]:

$$E_{\mathrm{UP,LP}}(\theta) = \frac{E_x + E_{\mathrm{ph}}(\theta)}{2} \pm \sqrt{V^2 + \frac{(E_x - E_{\mathrm{ph}}(\theta))^2}{4}}, \quad (1)$$

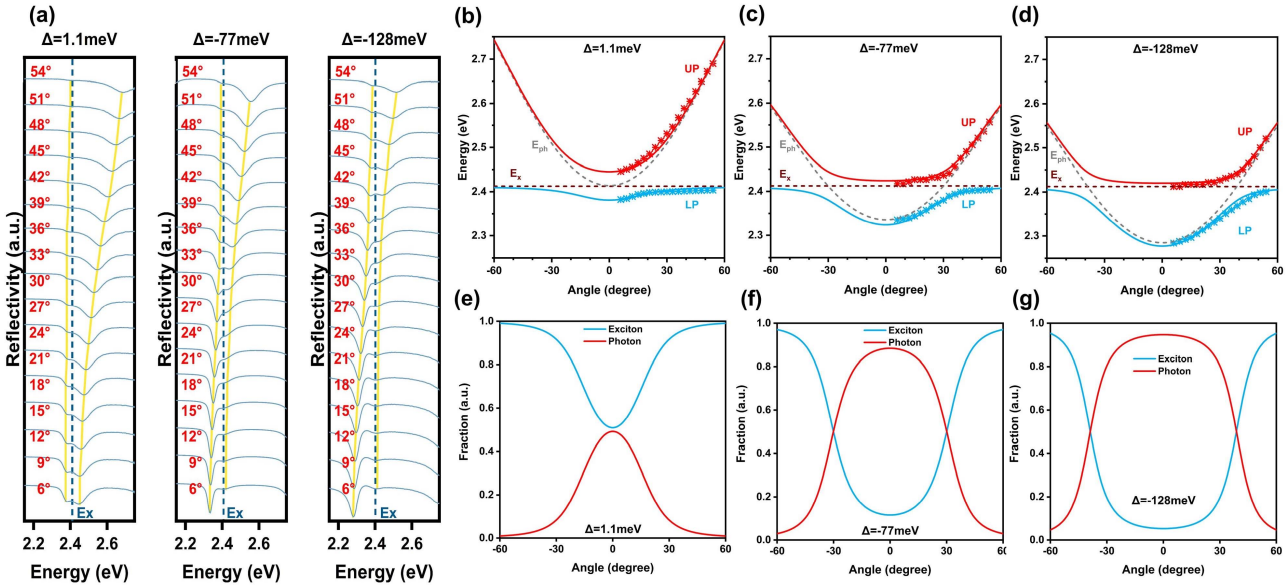

Fig. 2. Angle-resolved reflectivity and analysis. (a) Angle-resolved reflectivity (black lines) of devices at three different normal cavity–exciton detunings: $\Delta = 1.1$, −77, −128 meV and angle-dependent shifts of reflection dips (orange lines). (b)–(d) UP (red) and LP (blue) dispersion curves of exciton–polariton, fitted with extracted angle-resolved reflectivity dips (*) and theoretical two-level model (solid lines). Dotted lines correspond to the dispersion of the bare cavity photon (gray) and excitonic (purple) modes. (e)–(g) Components of exciton (blue) and photon (red) in LP states at the three detunings.

where E_{UP} and E_{LP} are the higher and lower energies corresponding to the two polariton branches, respectively, E_x is the energy of the exciton, $E_{ph}(\theta)$ is the energy dispersion of the bare cavity photon, and V is the coupling strength. Here, $E_{ph}(\theta) = E_{ph}(0°)/\sqrt{1 - (\sin(\theta)/n_{eff})^2}$, and n_{eff} is the effective refraction of the microcavity expressed in Eq. (C1) of Appendix C. E_x is regarded as a constant since the effective mass of the exciton is about 10^5 orders of magnitude larger than that of the photon [2]. $E_{ph}(0°)$ is determined by $E_{UP}(0°) + E_{LP}(0°) - E_x$. The detunings are defined as $\Delta = E_{ph}(0°) - E_x$, and the fitting results of three detunings ($\Delta = 1.1$, -77, -128 meV) are shown in Figs. 2(b)–2(d). The fitted polariton dispersions are in good agreement with experimental reflection data with a fitting parameter V of 32 meV. Therefore, the strong-coupling condition [44] ($\Omega > (\gamma_x + \gamma_{ph})/2$) is satisfied, where Ω is Rabi splitting energy ($\Omega = 2$ V, 64 meV), γ_x and γ_{ph} are the FWHMs of the exciton (75 meV from fitted excitonic absorption) and the cavity [36 meV from simulation of bare cavity in Appendix C Fig. 9(a)], respectively. At the crossing point of excitonic and photonic dispersion, the energy splits to higher ($E_x + V$) and lower ($E_x - V$) values. For nearly zero detuning, the crossing point lies at 0°, and the LP and UP exhibit the hybrid nature of an exciton and cavity photon at small angles. With increasing angles, the LP and UP dispersion tends towards excitonic and photonic behavior, respectively. For negative detunings, the LPs are photon-like and UPs are exciton-like at small angles. Beyond the hybrid crossing region of exciton and photon dispersion, the situation reverses at large angles. Undoubtedly, the anticrossing in the dispersion arises. To identify the excitonic and photonic fractions of polariton quantitatively, the Hopfield coefficients [2] of LP were calculated according to the formulas

$$|X|^2 = \frac{1}{2}\left(1 + \frac{E_{ph}(\theta) - E_x}{\sqrt{(E_{ph}(\theta) - E_x)^2 + 4V^2}}\right),$$
$$|C|^2 = \frac{1}{2}\left(1 - \frac{E_{ph}(\theta) - E_x}{\sqrt{(E_{ph}(\theta) - E_x)^2 + 4V^2}}\right), \quad (2)$$

where $|X|^2$ and $|C|^2$ represent the excitonic and photonic fractions, respectively. The results are shown in Figs. 2(e)–2(g), consistent with LP polariton dispersion. At the crossing point, both excitons and photons contribute equally, indicating a half-light half-matter superposition state of polaritons. At larger angles, the fraction of excitons tends to one, supporting that the LP tends to exciton dispersion. The photonic component dominates at small angles of negative detunings, confirming cavity-photon-like LP dispersion.

C. Photoluminescence and Electroluminescence Performances

The device results of our perovskite polariton LEDs are presented in Fig. 3. First, the angle-resolved PL (ARPL) and AREL spectra are displayed in Figs. 3(a)–3(c). The ARPL and AREL spectra are in good agreement and can be well fitted with the LP dispersion from ARR presented in Fig. 2. Interestingly, the ARPL and AREL tend to flatten at larger angles, in contrast to the parabolic-like cavity dispersion. Notably, the UP in ARPL and AREL cannot be observed, which can be attributed to the large Rabi splitting energy, high absorption above the bandgap of $CsPbBr_3$, and thermal relaxation to LP, similar to other reported perovskite strong-coupling microcavities [16,44,51]. Additionally, the ARPL and AREL of the device with −128 meV detuning display an accumulated emission in the range of 20° to 35°, indicating the presence of a bottleneck effect [44,53].

The LED performances are shown in Figs. 3(d)–3(i). The three-layer energy cascade structure NiO_x/TFB/PVK helps overcome an energy gap of about 0.9 eV between ITO and $CsPbBr_3$ [Fig. 3(d)] while avoiding fluorescence quenching. This structure is widely used in perovskite blue and green LEDs [47,54]. Electrons are injected into the $CsPbBr_3$ conduction band through the TPBi layer from the 30 nm MAA cathode. The reference LED device without a microcavity structure exhibits a peak EQE of 6.5% in Appendix C Figs. 8(a) and 8(b). It is noted here that we used much thicker $CsPbBr_3$ film than those commonly reported high-efficiency $CsPbBr_3$ LEDs to increase the excitonic absorption cross sections in the cavity, which might lead to unbalanced electron and hole injection, as discussed in Appendix C Fig. 8(c).

The *J-V-L*-EQE characteristics of our perovskite polariton LED with three detunings are compared in Figs. 3(e) and 3(f). All devices have a normal turn-on voltage of 2.6–2.8 V. Considering the nearly identical *J-V* curves and the different max luminance of 1152, 2311, and 2474 cd/m^2 for detunings of 1.1, −77, and −128 meV, the peak EQEs are calculated to 1.7%, 3.85%, and 3.7%, respectively. The lower EQE of the 1.1 meV detuning device may be due to the server self-absorption. The inset in Fig. 3(e) shows our device emitting bright green light under operation. The shape of the EL spectrum was almost unchanged when increasing current density from 3.33 to 33.3 mA/cm^2 as shown in Fig. 3(g), indicating the stability of the microcavity structure under different current injections. The EL FWHM of the 77 meV detuning device is 7.9 nm (35 meV). The statistics of the peak EQE of the fabricated devices in Fig. 3(h) demonstrate a centered distribution and good repeatability. Moreover, the T_{50} lifetime at an initial max luminance of 700 cd/m^2 is 6.4 min [Fig. 3(i)], at least ensuring that the device characteristic can be reliably measured.

D. Effect of Top Reflective MAA Electrode on the Device

The quality factor (Q) of a microcavity can be influenced by the reflectivity of the cavity mirror, as reported in previous studies [55,56]. In this section, we investigate the effect of changing the reflectivity of the top mirror by altering the thickness of the top metal electrode MAA. Specifically, we modified the thickness of the top-MAA cathode to 20 and 40 nm based on the −77 meV detuning device. The ARR spectra of the devices are presented in Fig. 4(a), and both devices exhibit two polariton dispersion branches. Notably, the reflection dips of the 40 nm MAA device are narrower and shallower than those of the 20 nm MAA device, indicating a higher reflectivity of the thicker mirror in a lossy cavity. The ARPL and AREL of the two devices are compared in Figs. 4(b) and 4(c), respectively. The angle-dependent emission fits well with the LP dispersion, and the coupling strength V is nearly the same for both devices, at approximately 32 meV. However, the detuning of the 40 nm

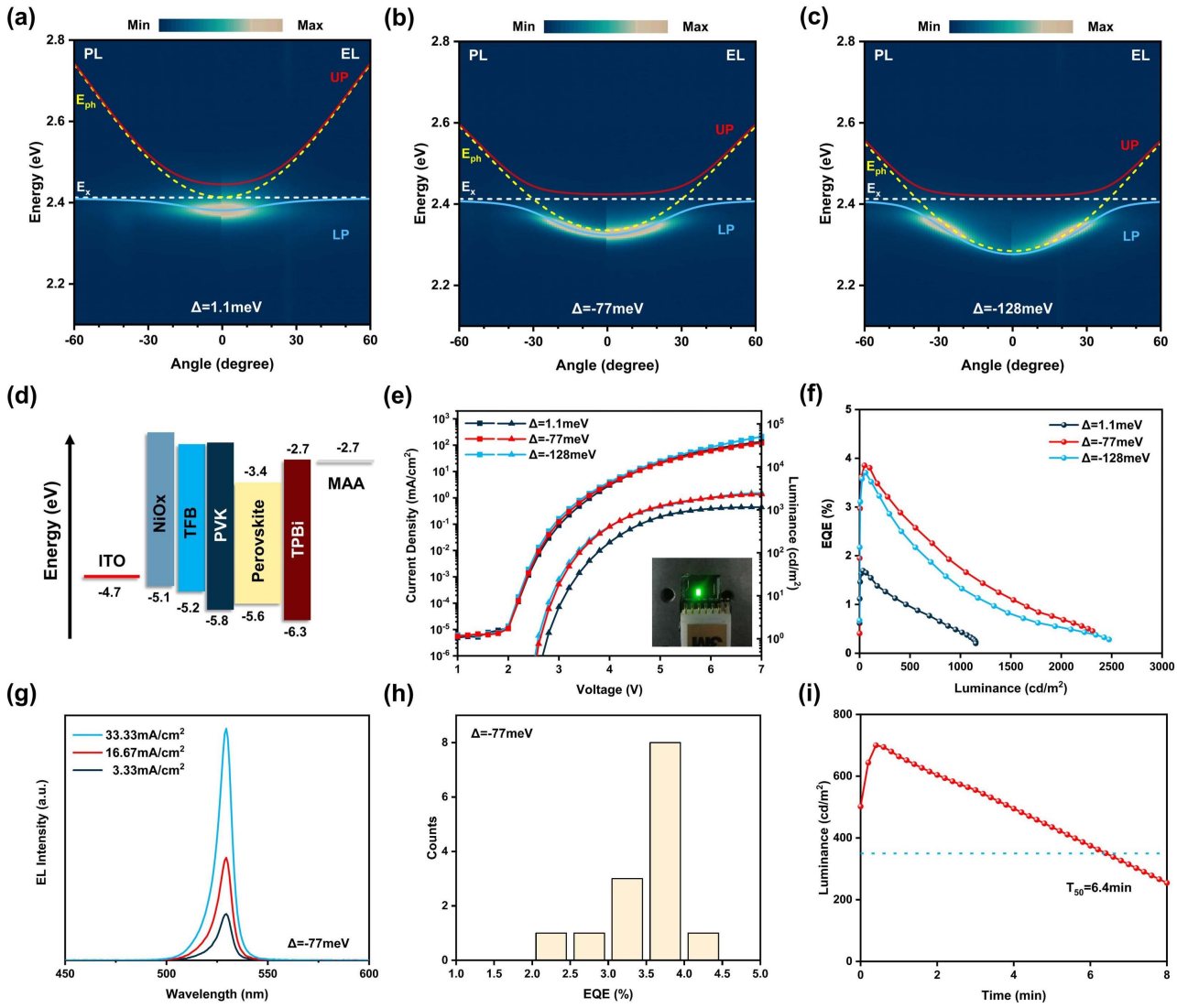

Fig. 3. Optoelectronic performance of the device. (a)–(c) Angle-resolved PL/EL spectra of the three detunings. UPs, LPs, E_x, and E_{ph} dispersions from fitted ARR in Fig. 2 are marked simultaneously. (d) Energy-level diagram of the as-fabricated device; (e), (f) comparison of current density(J)-voltage(V)-luminance(L)-external quantum efficiency (EQE) curves (inset: photograph of perovskite exciton–polariton LED at operation); (g) spectral stability of the −77 meV detuning device under different current densities; (h) distribution of peak EQE for −77 meV detuning devices; (i) operational stability of the −77 meV detuning device under constant current measured with an initial max luminance of 700 cd/cm^2.

MAA device is shifted to −50 meV. This phenomenon is supported by the simulation of a bare cavity, as shown in Appendix C Figs. 9(b) and 9(c). The simulation indicates that the thicker metal mirror reduces the metal reflective phase shift and leads to the reducing total optical thickness of the cavity, resulting in a blueshift of the resonance wavelength according to the resonance condition [57]. Regarding the LED performances, the 20 nm MAA device shows a maximum luminance of 3526 cd/m^2 and peak EQE of 5.37%, while the 40 nm MAA device exhibits a maximum luminance of 2346 cd/m^2 and peak EQE of 2%, as presented in Figs. 4(d) and 4(e). The difference in EQE can be attributed to the outcoupling efficiency, which is influenced by the thickness of the top metal electrode. Benefiting from the high Q value of the 40 nm MAA-based microcavity, the FWHM of EL is narrowed to 6.5 nm (28.3 meV), which is about half that of the 20 nm MAA device (12.6 nm, 56.2 meV), as shown in Fig. 4(f). Therefore, there is a trade-off between high EQE and narrow spectral width for microcavity polariton LEDs. Interestingly, the 6.5 nm EL FWHM is the narrowest bandwidth for spin-coated perovskite LEDs reported so far.

Although we have demonstrated that perovskite polariton LEDs can work in the strong-coupling regime under RT, the current density required to reach the threshold of Bose–Einstein condensation for coherent lasing emission is still far from being achieved. With the rapid development of perovskite LEDs [58–63], we can anticipate a more stable and efficient perovskite polariton LED that bears higher current injections. The Q factors can certainly be improved not only by improving the reflection of mirrors employing double DBRs, but also

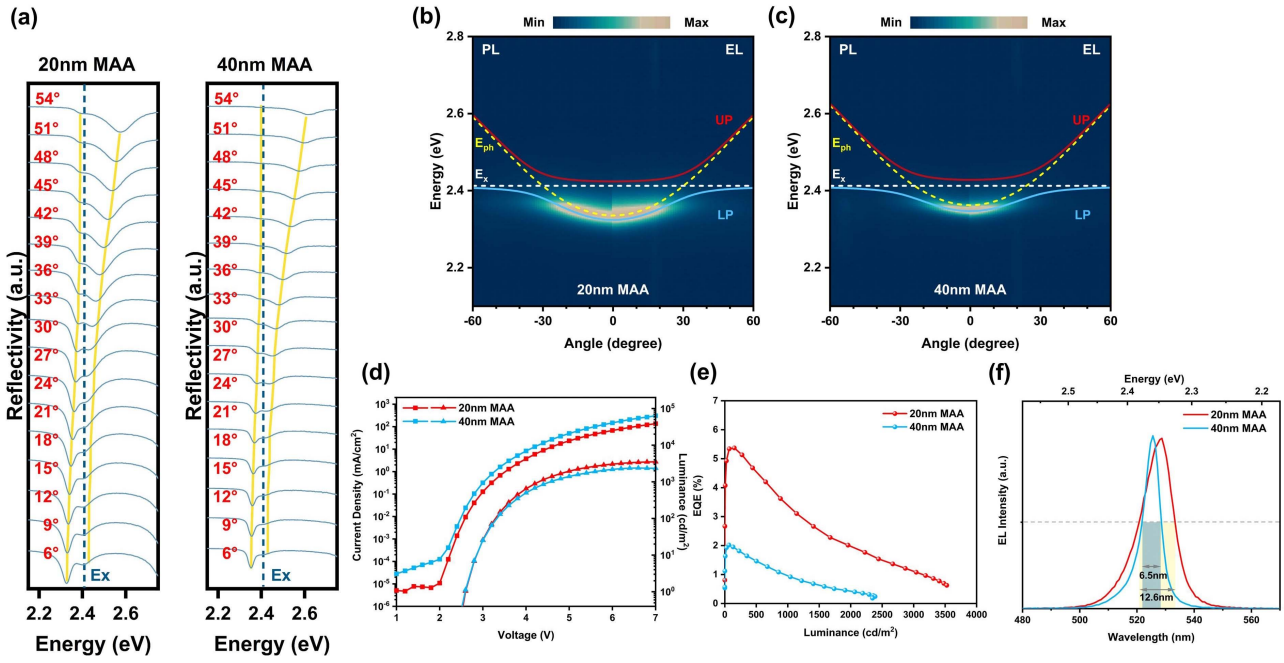

Fig. 4. Influence of MAA electrode thickness on device performance. (a) Angle-resolved reflectivity of devices with 20 and 40 nm MAA as top electrodes; (b), (c) angle-resolved PL/EL of devices with 20 and 40 nm MAA as top electrodes; (d), (e) *J-V-L*-EQE characteristics; (f) normal EL spectra with 20 and 40 nm MAA electrodes.

by reducing the optical losses by optimizing film morphologies and electrical injection structure. As for the gain material, though low-dimensional perovskite generally has larger exciton binding energy, we are still more favorable for the three-dimensional perovskite that intrinsically has better mobility and phase purity. With the collaborative efforts from both device and material sides, we believe the electrically pumped perovskite polariton laser will be ultimately realized.

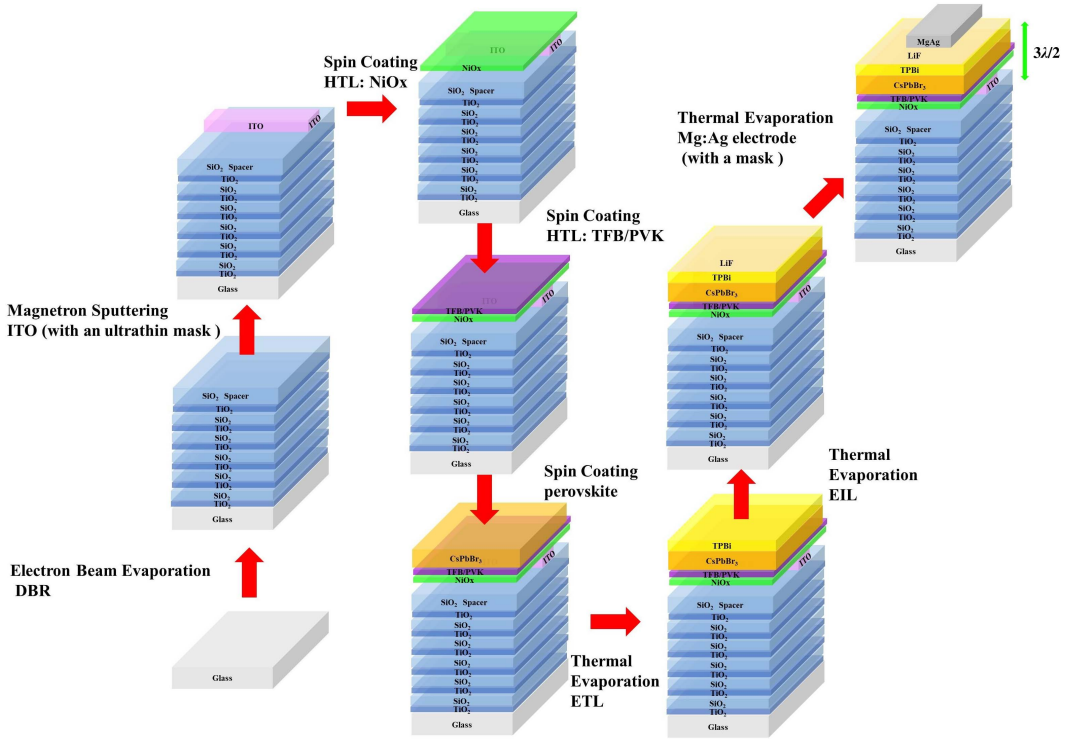

Fig. 5. Fabrication process of our perovskite polariton LED.

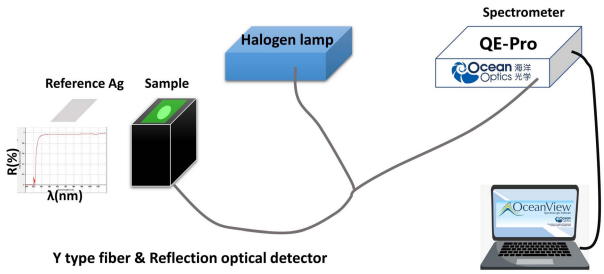

Fig. 6. Schematic diagram of normal reflection detection.

4. CONCLUSION

In conclusion, we have successfully demonstrated the operation of RT solution-processed perovskite polariton LEDs by combining a solution-processed $CsPbBr_3$ LED with a metal–dielectric microcavity. The prepared $CsPbBr_3$ film displayed a distinct excitonic characteristic at the band edge and maintained a good luminescence capacity. We confirmed the strong coupling regime through dispersion relation analysis from angle-resolved reflectivity measurements, with a Rabi splitting energy of 64 meV. Moreover, AREL and ARPL with different detunings followed the LP branch dispersion. Our perovskite polariton LEDs exhibited external quantum efficiencies (EQEs) of 1.7%, 3.85%, and 3.7% for 1.1, −77, and −128 meV detunings, respectively, with maximum luminance of 1152, 2311, and 2474 cd/m^2. Further explorations on the reflection of the metal mirror lead to a device with higher efficiency of 5.34% and a device with a narrower emission bandwidth of 6.5 nm. We have made groundbreaking progress by developing RT perovskite polariton LEDs that are compatible with widely used solution-processed perovskite device technology. However, there is still room for improvement in terms of enhancing device performance, achieving electrically pumped perovskite polariton

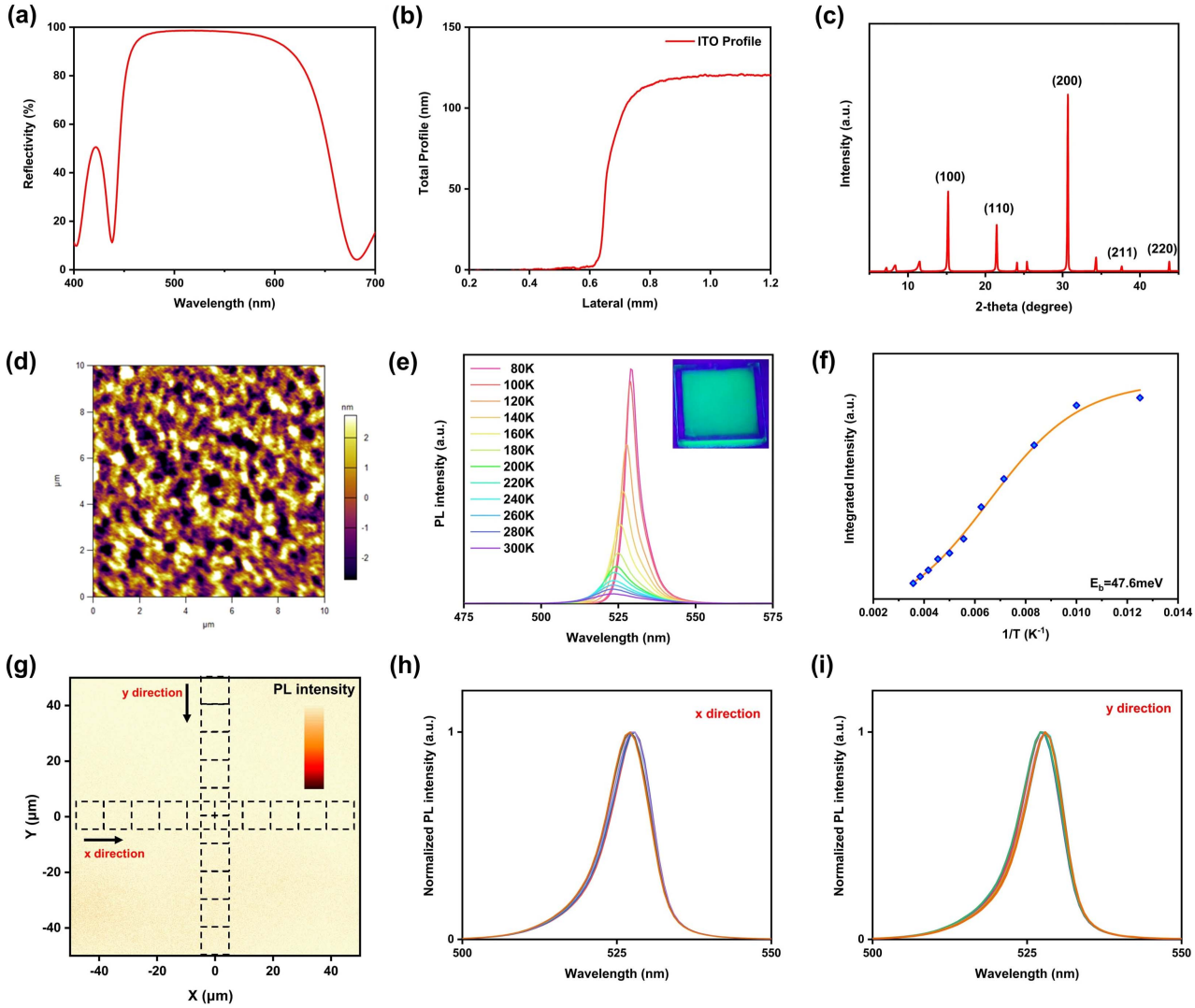

Fig. 7. Additional reliability data of device fabrication. (a) Reflection of TiO_2/SiO_2 substrate. (b) Edge of ITO film sputtered with a 0.1 mm thick mask. (c) XRD pattern for the prepared $CsPbBr_3$ film. (d) AFM topography image of the prepared $CsPbBr_3$ film. The root mean square (RMS) roughness is 1.737 nm. (e) Temperature-dependent photoluminescence of prepared $CsPbBr_3$ film; the inset is a photograph of prepared $CsPbBr_3$ film under UV light illumination. (f) Integrated photoluminescence intensities are fitted by $I(T) = I_0/(1 + A \cdot \exp(-E_b/KT))$ [47,48]. Exciton binding energy is extracted from fitting parameter E_b. (g)–(i) PL spectra of x direction and y direction square subregions.

condensation, and developing other types of electrically injected perovskite polariton devices that can operate at RT.

APPENDIX A

In this section, we provide two schematics: the fabrication process of our perovskite polariton LED in Fig. 5 and the setup of normal reflection detection in Fig. 6.

APPENDIX B

In this section, we provide some additional fabrication reliability data in Fig. 7.

APPENDIX C

In this section, we provide performances of the reference LED device in Figs. 8(a) and 8(b), electrical properties of single-carrier devices in Fig. 8(c), calculation methods of effective refractive index in Eq. (C1), and simulation of bare cavity reflection in Fig. 9.

The effective refractive index n_{eff} is expressed by

$$n_{\text{eff}} = \frac{n_{\text{DBR}} L_{\text{DBR}} + \sum n_i d_i}{L_{\text{DBR}} + \sum d_i}, \tag{C1}$$

where n_i, d_i are the refractive index and thickness of each layer inside the microcavity, and n_{DBR}, L_{DBR} are the effective refractive index and penetration length for DBR expressed in Ref. [44], respectively.

Funding. National Key Research and Development Program of China (2017YFA0207700); Outstanding Youth Fund of Zhejiang Natural Science Foundation (LR18F050001); National Natural Science Foundation of China (61804134, 61874096, 62074136).

Disclosures. The authors declare no conflicts of interest.

Data Availability. Data underlying the results presented in this paper are not publicly available at this time but may be obtained from the authors upon reasonable request.

REFERENCES

1. R. Su, A. Fieramosca, Q. Zhang, H. S. Nguyen, E. Deleporte, Z. Chen, D. Sanvitto, T. C. H. Liew, and Q. Xiong, "Perovskite semiconductors for room-temperature exciton-polaritonics," Nat. Mater. **20**, 1315–1324 (2021).
2. H. Deng, H. Haug, and Y. Yamamoto, "Exciton-polariton Bose-Einstein condensation," Rev. Mod. Phys. **82**, 1489–1537 (2010).

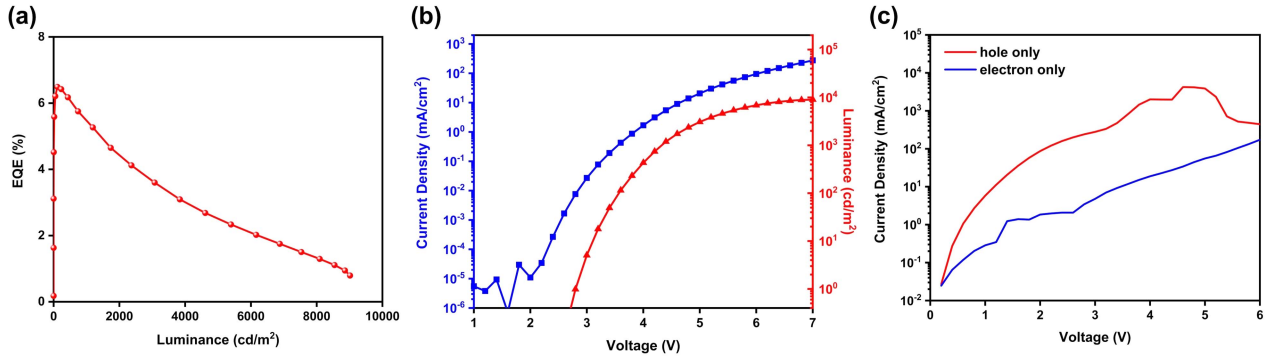

Fig. 8. (a), (b) *J*-*V*-*L*-EQE characteristics of reference LED without microcavity. (c) Current density versus voltage curves of hole-only and electron-only devices.

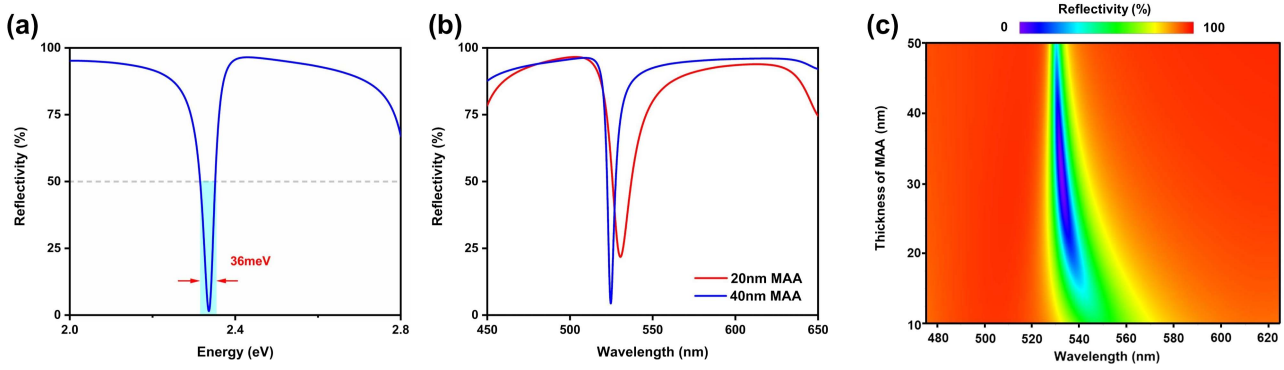

Fig. 9. (a) Simulation of bare cavity reflectivity. The FWHM of cavity mode is 36 meV. (b) Comparison of simulated reflection of bare cavity with 20 and 40 nm MAA top electrode. (c) Simulated reflection of cavity mode with thickness of MAA from 10 to 50 nm.

3. S. Ghosh, R. Su, J. Zhao, A. Fieramosca, J. Wu, T. Li, Q. Zhang, F. Li, Z. Chen, T. Liew, D. Sanvitto, and Q. Xiong, "Microcavity exciton polaritons at room temperature," Photon. Insights **1**, R04 (2022).
4. D. Sanvitto and S. Kena-Cohen, "The road towards polaritonic devices," Nat. Mater. **15**, 1061–1073 (2016).
5. D. Ballarini, M. De Giorgi, E. Cancellieri, R. Houdre, E. Giacobino, R. Cingolani, A. Bramati, G. Gigli, and D. Sanvitto, "All-optical polariton transistor," Nat. Commun. **4**, 1778 (2013).
6. C. Schneider, A. Rahimi-Iman, N. Y. Kim, J. Fischer, I. G. Savenko, M. Amthor, M. Lermer, A. Wolf, L. Worschech, V. D. Kulakovskii, I. A. Shelykh, M. Kamp, S. Reitzenstein, A. Forchel, Y. Yamamoto, and S. Höfling, "An electrically pumped polariton laser," Nature **497**, 348–352 (2013).
7. C. Sturm, D. Tanese, H. S. Nguyen, H. Flayac, E. Galopin, A. Lemaitre, I. Sagnes, D. Solnyshkov, A. Amo, G. Malpuech, and J. Bloch, "All-optical phase modulation in a cavity-polariton Mach-Zehnder interferometer," Nat. Commun. **5**, 3278 (2014).
8. Y. Xue, I. Chestnov, E. Sedov, E. Kiktenko, A. K. Fedorov, S. Schumacher, X. Ma, and A. Kavokin, "Split-ring polariton condensates as macroscopic two-level quantum systems," Phys. Rev. Res. **3**, 013099 (2021).
9. Y. Higuchi, K. Omae, H. Matsumura, and T. Mukai, "Room-temperature CW lasing of a GaN-based vertical-cavity surface-emitting laser by current injection," Appl. Phys. Express **1**, 121102 (2008).
10. P. G. Savvidis, "A practical polariton laser," Nat. Photonics **8**, 588–589 (2014).
11. I. D. W. Samuel, E. B. Namdas, and G. A. Turnbull, "How to recognize lasing," Nat. Photonics **3**, 546–549 (2009).
12. H. Deng, G. Weihs, D. Snoke, J. Bloch, and Y. Yamamoto, "Polariton lasing vs. photon lasing in a semiconductor microcavity," Proc. Natl. Acad. Sci. USA **100**, 15318–15323 (2003).
13. T. Byrnes, N. Y. Kim, and Y. Yamamoto, "Exciton–polariton condensates," Nat. Phys. **10**, 803–813 (2014).
14. H. Kim, L. Zhao, J. S. Price, A. J. Grede, K. Roh, A. N. Brigeman, M. Lopez, B. P. Rand, and N. C. Giebink, "Hybrid perovskite light emitting diodes under intense electrical excitation," Nat. Commun. **9**, 4893 (2018).
15. C. Zou, Y. Liu, D. S. Ginger, and L. Y. Lin, "Suppressing efficiency roll-off at high current densities for ultra-bright green perovskite light-emitting diodes," ACS Nano **14**, 6076–6086 (2020).
16. R. Su, C. Diederichs, J. Wang, T. C. H. Liew, J. Zhao, S. Liu, W. Xu, Z. Chen, and Q. Xiong, "Room-temperature polariton lasing in all-inorganic perovskite nanoplatelets," Nano Lett. **17**, 3982–3988 (2017).
17. W. Du, S. Zhang, J. Shi, J. Chen, Z. Wu, Y. Mi, Z. Liu, Y. Li, X. Sui, R. Wang, X. Qiu, T. Wu, Y. Xiao, Q. Zhang, and X. Liu, "Strong exciton–photon coupling and lasing behavior in all-inorganic $CsPbBr_3$ micro/nanowire Fabry-Pérot cavity," ACS Photon. **5**, 2051–2059 (2018).
18. Q. Shang, M. Li, L. Zhao, D. Chen, S. Zhang, S. Chen, P. Gao, C. Shen, J. Xing, G. Xing, B. Shen, X. Liu, and Q. Zhang, "Role of the exciton-polariton in a continuous-wave optically pumped $CsPbBr_3$ perovskite laser," Nano Lett. **20**, 6636–6643 (2020).
19. R. Su, J. Wang, J. Zhao, J. Xing, W. Zhao, C. Diederichs, T. C. H. Liew, and Q. Xiong, "Room temperature long-range coherent exciton polariton condensate flow in lead halide perovskites," Sci. Adv. **4**, eaau0244 (2018).
20. K. Peng, R. Tao, L. Haeberle, Q. Li, D. Jin, G. R. Fleming, S. Kena-Cohen, X. Zhang, and W. Bao, "Room-temperature polariton quantum fluids in halide perovskites," Nat. Commun. **13**, 7388 (2022).
21. L. Polimeno, A. Fieramosca, G. Lerario, M. Cinquino, M. De Giorgi, D. Ballarini, F. Todisco, L. Dominici, V. Ardizzone, M. Pugliese, C. T. Prontera, V. Maiorano, G. Gigli, L. De Marco, and D. Sanvitto, "Observation of two thresholds leading to polariton condensation in 2D hybrid perovskites," Adv. Opt. Mater. **8**, 2000176 (2020).
22. M. S. Spencer, Y. Fu, A. P. Schlaus, D. Hwang, Y. Dai, M. D. Smith, D. R. Gamelin, and X. Y. Zhu, "Spin-orbit-coupled exciton-polariton condensates in lead halide perovskites," Sci. Adv. **7**, eabj7667 (2021).
23. R. Tao, K. Peng, L. Haeberlé, Q. Li, D. Jin, G. R. Fleming, S. Kéna-Cohen, X. Zhang, and W. Bao, "Halide perovskites enable polaritonic XY spin Hamiltonian at room temperature," Nat. Mater. **21**, 761–766 (2022).
24. R. Su, S. Ghosh, J. Wang, S. Liu, C. Diederichs, T. C. H. Liew, and Q. Xiong, "Observation of exciton polariton condensation in a perovskite lattice at room temperature," Nat. Phys. **16**, 301–306 (2020).
25. J. Wang, H. Xu, R. Su, Y. Peng, J. Wu, T. C. H. Liew, and Q. Xiong, "Spontaneously coherent orbital coupling of counterrotating exciton polaritons in annular perovskite microcavities," Light Sci. Appl. **10**, 45 (2021).
26. J. Wu, R. Su, A. Fieramosca, S. Ghosh, J. Zhao, T. C. H. Liew, and Q. Xiong, "Perovskite polariton parametric oscillator," Adv. Photon. **3**, 055003 (2021).
27. D. Bajoni, E. Semenova, A. Lemaître, S. Bouchoule, E. Wertz, P. Senellart, and J. Bloch, "Polariton light-emitting diode in a GaAs-based microcavity," Phys. Rev. B **77**, 113303 (2008).
28. S. I. Tsintzos, N. T. Pelekanos, G. Konstantinidis, Z. Hatzopoulos, and P. G. Savvidis, "A GaAs polariton light-emitting diode operating near room temperature," Nature **453**, 372–375 (2008).
29. S. I. Tsintzos, P. G. Savvidis, G. Deligeorgis, Z. Hatzopoulos, and N. T. Pelekanos, "Room temperature GaAs exciton-polariton light emitting diode," Appl. Phys. Lett. **94**, 071109 (2009).
30. S. Brodbeck, J. P. Jahn, A. Rahimi-Iman, J. Fischer, M. Amthor, S. Reitzenstein, M. Kamp, C. Schneider, and S. Höfling, "Room temperature polariton light emitting diode with integrated tunnel junction," Opt. Express **21**, 31098–31104 (2013).
31. T. C. Lu, J. R. Chen, S. C. Lin, S. W. Huang, S. C. Wang, and Y. Yamamoto, "Room temperature current injection polariton light emitting diode with a hybrid microcavity," Nano Lett. **11**, 2791–2795 (2011).
32. Z. Zhang, Y. Wang, S. Yin, T. Hu, Y. Wang, L. Liao, S. Luo, J. Wang, X. Zhang, P. Ni, X. Shen, C. Shan, and Z. Chen, "Exciton-polariton light-emitting diode based on a ZnO microwire," Opt. Express **25**, 17375–17381 (2017).
33. M. Jiang, K. Tang, P. Wan, T. Xu, H. Xu, and C. Kan, "A single microwire near-infrared exciton–polariton light-emitting diode," Nanoscale **13**, 1663–1672 (2021).
34. F. Zhang, K. Tang, P. Wan, C. Kan, and M. Jiang, "An electrically driven single microribbon based near-infrared exciton–polariton light-emitting diode," CrystEngComm **23**, 4336–4343 (2021).
35. M. Liu, M. Jiang, Q. Zhao, K. Tang, S. Sha, B. Li, C. Kan, and D. N. Shi, "Ultraviolet exciton-polariton light-emitting diode in a ZnO microwire homojunction," ACS Appl. Mater. Interfaces **15**, 13258–13269 (2023).
36. H. Xu, J. Xu, M. Jiang, M. Liu, K. Tang, C. Kan, and D. Shi, "Exciton-polariton light-emitting diode based on a single ZnO superlattice microwire heterojunction with performance enhanced by Rh nanostructures," Phys. Chem. Chem. Phys. **25**, 5836–5848 (2023).
37. N. Christogiannis, N. Somaschi, P. Michetti, D. M. Coles, P. G. Savvidis, P. G. Lagoudakis, and D. G. Lidzey, "Characterizing the electroluminescence emission from a strongly coupled organic semiconductor microcavity LED," Adv. Opt. Mater. **1**, 503–509 (2013).
38. M. Mazzeo, A. Genco, S. Gambino, D. Ballarini, F. Mangione, O. Di Stefano, S. Patanè, S. Savasta, D. Sanvitto, and G. Gigli, "Ultrastrong light-matter coupling in electrically doped microcavity organic light emitting diodes," Appl. Phys. Lett. **104**, 233303 (2014).
39. A. Genco, A. Ridolfo, S. Savasta, S. Patanè, G. Gigli, and M. Mazzeo, "Bright polariton Coumarin-based OLEDs operating in the ultrastrong coupling regime," Adv. Opt. Mater. **6**, 1800364 (2018).
40. J. F. Chang, T. Y. Lin, C. F. Hsu, S. Y. Chen, S. Y. Hong, G. S. Ciou, C. C. Jaing, and C. C. Lee, "Development of a highly efficient, strongly coupled organic light-emitting diode based on intracavity pumping architecture," Opt. Express **28**, 39781–39789 (2020).
41. J. F. Chang, Y. C. Zheng, C. Y. Chiang, C. K. Huang, and C. C. Jaing, "Ultrastrong coupling in super yellow polymer microcavities and development of highly efficient polariton light-emitting diodes and light-emitting transistors," Opt. Express **31**, 6849–6861 (2023).
42. J. Gu, B. Chakraborty, M. Khatoniar, and V. M. Menon, "A room-temperature polariton light-emitting diode based on monolayer WS_2," Nat. Nanotechnol. **14**, 1024–1028 (2019).
43. T. Wang, Z. Zang, Y. Gao, C. Lyu, P. Gu, Y. Yao, K. Peng, K. Watanabe, T. Taniguchi, X. Liu, Y. Gao, W. Bao, and Y. Ye, "Electrically pumped polarized exciton-polaritons in a halide perovskite microcavity," Nano Lett. **22**, 5175–5181 (2022).

44. P. Bouteyre, H. S. Nguyen, J. S. Lauret, G. Trippe-Allard, G. Delport, F. Ledee, H. Diab, A. Belarouci, C. Seassal, D. Garrot, F. Bretenaker, and E. Deleporte, "Room-temperature cavity polaritons with 3D hybrid perovskite: toward large-surface polaritonic devices," ACS Photon. **6**, 1804–1811 (2019).
45. T. Liu, C. Yang, Z. Fan, X. Chen, Z. Chen, Y. Su, H. Zhu, F. Sun, T. Jiang, W. Zhu, W. Shen, J. He, H. Zhu, X. Liu, and Y. Yang, "Spectral narrowing and enhancement of directional emission of perovskite light emitting diode by microcavity," Laser Photon. Rev. **16**, 2200091 (2022).
46. G. F. Burkhard, E. T. Hoke, and M. D. McGehee, "Accounting for interference, scattering, and electrode absorption to make accurate internal quantum efficiency measurements in organic and other thin solar cells," Adv. Mater. **22**, 3293–3297 (2010).
47. T. Wu, J. Li, Y. Zou, H. Xu, K. Wen, S. Wan, S. Bai, T. Song, J. A. McLeod, S. Duhm, F. Gao, and B. Sun, "High-performance perovskite light-emitting diode with enhanced operational stability using lithium halide passivation," Angew. Chem. Int. Ed. **59**, 4099–4105 (2020).
48. P. Du, J. Li, L. Wang, L. Sun, X. Wang, X. Xu, L. Yang, J. Pang, W. Liang, J. Luo, Y. Ma, and J. Tang, "Efficient and large-area all vacuum-deposited perovskite light-emitting diodes via spatial confinement," Nat. Commun. **12**, 4751 (2021).
49. S. K. Kwon, E. H. Lee, K. S. Kim, H. C. Choi, M. J. Park, S. K. Kim, R. Pode, and J. H. Kwon, "Efficient micro-cavity top emission OLED with optimized Mg:Ag ratio cathode," Opt. Express **25**, 29906–29915 (2017).
50. C. Zang, S. Liu, M. Xu, R. Wang, C. Cao, Z. Zhu, J. Zhang, H. Wang, L. Zhang, W. Xie, and C. S. Lee, "Top-emitting thermally activated delayed fluorescence organic light-emitting devices with weak light-matter coupling," Light Sci. Appl. **10**, 116 (2021).
51. J. Wang, R. Su, J. Xing, D. Bao, C. Diederichs, S. Liu, T. C. H. Liew, Z. Chen, and Q. Xiong, "Room temperature coherently coupled exciton-polaritons in two-dimensional organic-inorganic perovskite," ACS Nano **12**, 8382–8389 (2018).
52. C. Ouyang, Y. Li, X. Fu, Z. Zeng, L. Huang, S. Liu, X. Wang, T. Gao, and A. Pan, "Room temperature exciton-polaritons in high-quality 2D Ruddlesden–Popper perovskites (BA)2(MA)n-1PbnI3n+1 (n = 3, 4)," Appl. Phys. Lett. **117**, 221107 (2020).
53. F. Tassone, C. Piermarocchi, V. Savona, A. Quattropani, and P. Schwendimann, "Bottleneck effects in the relaxation and photoluminescence of microcavity polaritons," Phys. Rev. B **56**, 7554–7563 (1997).
54. Y. Liu, J. Cui, K. Du, H. Tian, Z. He, Q. Zhou, Z. Yang, Y. Deng, D. Chen, X. Zuo, Y. Ren, L. Wang, H. Zhu, B. Zhao, D. Di, J. Wang, R. H. Friend, and Y. Jin, "Efficient blue light-emitting diodes based on quantum-confined bromide perovskite nanostructures," Nat. Photonics **13**, 760–764 (2019).
55. L. Wang, J. Lin, Y. Lv, B. Zou, J. Zhao, and X. Liu, "Red, green, and blue microcavity quantum dot light-emitting devices with narrow line widths," ACS Appl. Nano Mater. **3**, 5301–5310 (2020).
56. J. Lin, Y. Hu, and X. Liu, "Microcavity-enhanced blue organic light-emitting diode for high-quality monochromatic light source with nonquarterwave structural design," Adv. Opt. Mater. **8**, 1901421 (2020).
57. A. Dodabalapur, L. J. Rothberg, R. H. Jordan, T. M. Miller, R. E. Slusher, and J. M. Phillips, "Physics and applications of organic microcavity light emitting diodes," J. Appl. Phys. **80**, 6954–6964 (1996).
58. K. Lin, J. Xing, L. N. Quan, F. P. G. de Arquer, X. Gong, J. Lu, L. Xie, W. Zhao, D. Zhang, C. Yan, W. Li, X. Liu, Y. Lu, J. Kirman, E. H. Sargent, Q. Xiong, and Z. Wei, "Perovskite light-emitting diodes with external quantum efficiency exceeding 20 per cent," Nature **562**, 245–248 (2018).
59. L. Zhang, F. Yuan, J. Xi, B. Jiao, H. Dong, J. Li, and Z. Wu, "Suppressing ion migration enables stable perovskite light-emitting diodes with all-inorganic strategy," Adv. Funct. Mater. **30**, 2001834 (2020).
60. Z. Liu, W. Qiu, X. Peng, G. Sun, X. Liu, D. Liu, Z. Li, F. He, C. Shen, Q. Gu, F. Ma, H. L. Yip, L. Hou, Z. Qi, and S. J. Su, "Perovskite light-emitting diodes with EQE exceeding 28% through a synergetic dual-additive strategy for defect passivation and nanostructure regulation," Adv. Mater. **33**, 2103268 (2021).
61. D. Ma, K. Lin, Y. Dong, H. Choubisa, A. H. Proppe, D. Wu, Y.-K. Wang, B. Chen, P. Li, J. Z. Fan, F. Yuan, A. Johnston, Y. Liu, Y. Kang, Z.-H. Lu, Z. Wei, and E. H. Sargent, "Distribution control enables efficient reduced-dimensional perovskite LEDs," Nature **599**, 594–598 (2021).
62. S.-J. Woo, J. S. Kim, and T.-W. Lee, "Characterization of stability and challenges to improve lifetime in perovskite LEDs," Nat. Photonics **15**, 630–634 (2021).
63. J. S. Kim, J.-M. Heo, G.-S. Park, S.-J. Woo, C. Cho, H. J. Yun, D.-H. Kim, J. Park, S.-C. Lee, S.-H. Park, E. Yoon, N. C. Greenham, and T.-W. Lee, "Ultra-bright, efficient and stable perovskite light-emitting diodes," Nature **611**, 688–694 (2022).